ACS APPLIED NANO MATERIALS

www.acsanm.org

Article

Laser-Controlled Growth of Plasmonic Gold Nanoparticles in PMMA Films for High-Resolution Optical Applications

Richard Silveira Pereira, Diego Lourençoni Ferreira, Gabriel Ferrari de Oliveira, Gabriele C. Felipe de Paula, André Luís dos Santos Romero, Cleber Renato Mendonça, and Marcelo Gonçalves Vivas*

Cite This: ACS Appl. Nano Mater. 2025, 8, 8294−8306

Read Online

ACCESS | Metrics & More | Article Recommendations | Supporting Information

ABSTRACT: The growing demand for portable electronics has driven advancements in micro- and nanoscale technologies. In this regard, plasmonic nanomaterials are particularly notable for their capacity to manipulate surface plasmons, enabling applications in super-resolution microscopy, optical nanosensors, cancer therapy, and high-resolution displays, among other fields. This work aims to control the size, concentration, density, and shape anisotropy of gold nanoparticles (AuNPs) while generating plasmonic platforms in poly(methyl methacrylate) (PMMA) films, controlling the laser power and translation speed during the direct laser writing technique. The nucleation and growth processes of AuNPs in PMMA films were explained using the laser-induced plasma classical model. Using a computational method based on the Mie-Gans approach, we identified nanoparticles with diameters ranging from 2 to 30 nm, concentrations varying from 0.9 μM to 1.9 mM, aspect ratio values between 1.1 and 1.5, and density like the bulk gold and plasmonic microstructures with widths spanning from 5 to 70 μm. Additionally, areas of the film with the highest nanoparticle density were mapped using rhodamine B fluorescence, which varied according to laser power. The results demonstrate that gold nanoparticles can be generated with high precision in polymers at a micrometer resolution with high chemical stability, making this technique versatile and cost-effective compared to traditional methods.

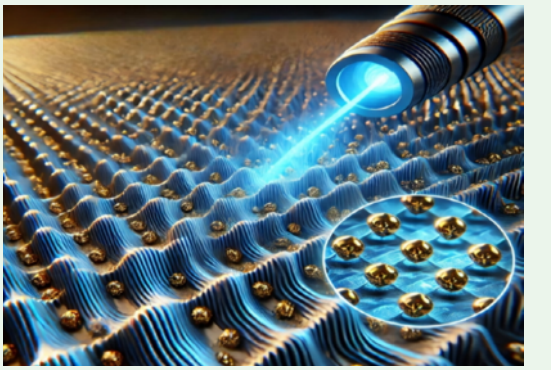

KEYWORDS: *laser-controlled growth, plasmonic nanomaterials, Mie-Gans approach, PMMA, high-resolution optical applications*

1. INTRODUCTION

Metal nanoparticles have been used in various scientific fields, contributing to the development of innovative technologies. These unique features are attributed mainly to their ability to generate surface plasmons, which find applications in areas such as super-resolution microscopy,[1−3] optical nanosensors,[4−7] cancer therapy,[8,9] and high-resolution displays,[10−13] among others.[14−17] Localized surface plasmons (LSPs) are collective electron oscillations that occur in the interface between a metallic nanostructure and a dielectric medium.[18,19] In this case, plasmons can be directly excited by unpolarized light with a wavelength significantly higher than the nanostructure size, making them particularly suitable for sensing and biomedical applications.[20−23] However, a significant challenge lies in obtaining precise control over the physicochemical parameters of plasmonic structures, such as size, shape, and concentration of metal nanoparticles within organic substrates, limiting their integration in optoelectronic devices.[24−29]

Conventional fabrication techniques, such as photolithography and electron-beam lithography, offer high precision but present high costs associated with scaling up production, are limited to the 2D structure fabrication, and require complex masking processes.[30−36] To overcome these limitations, alternative methods, such as direct laser writing (DLW), have been developed to fabricate 2D/3D nano- and microstructures in a single step without mechanical contact or complex environmental controls.[37−40] DLW has shown to be a promising technique for creating metallic nanostructures in organic and semiconductor substrates.[41,42] Also, the DLW has been employed to fabricate plasmonic microstructure from the metalloid gold nanocluster as a precursor material, offering a fast and reliable method.[43,44] On the other hand, systematic studies quantifying the influence of DLW fabrication parameters on nanoparticle physicochemical properties are scarce. This gap restricts the ability to tailor plasmonic

Received: February 10, 2025
Revised: April 4, 2025
Accepted: April 7, 2025
Published: April 11, 2025

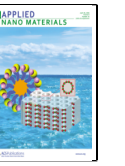

materials for specific applications, particularly optoelectronics and sensing applications.

Poly(methyl methacrylate) (PMMA), a widely used dielectric polymer, offers an ideal platform for integrating metal nanoparticles due to its optical transparency, mechanical robustness, and compatibility with various fabrication techniques and nonlinear optical systems.[45−49] It also shows significant potential as a protective coating for perovskite thin films, enhancing the performance and durability of optoelectronic devices such as solar cells, lasers, and LEDs.[50−54] However, the synthesis of metal nanoparticles within PMMA matrices with precise control over their physicochemical properties has not been thoroughly explored, primarily due to challenges in characterizing nanoparticles embedded in polymers using transmission electron microscopy (TEM).

Herein, we have addressed these challenges by employing the DLW technique to fabricate gold nanoparticles (AuNPs) within PMMA films containing a metal precursor (tetrachloroauric acid trihydrate ($HAuCl_4{\cdot}3H_2O$), using a continuous-wave (cw) laser at 405 nm. By systematically varying laser power and translation speed, we achieve precise control over the size, shape anisotropy, concentration and density of AuNPs, enabling the fine-tuning of their plasmonic properties. The AuNPs physicochemical properties are quantitatively analyzed using a computational program based on the Mie-Gans approach.[18,19,55] This work demonstrates the feasibility of DLW as a cost-effective and versatile alternative to conventional lithography and provides a framework for designing plasmonic materials with tailored optical responses for advanced optoelectronic and sensing applications.

2. EXPERIMENTAL SECTION

2.1. Materials. Poly(methyl methacrylate) (PMMA), tetrachloroauric acid trihydrate ($HAuCl_4{\cdot}3H_2O$, 393.83 g·mol^{-1}) and rhodamine B (479.01 g·mol^{-1}) were purchased from Sigma-Aldrich. Chloroform ($CHCl_3$, 119.38 g·mol^{-1}) was acquired from Labsynth. All chemicals were used as received.

2.2. Fabrication of PMMA Films. The first step involved the fabrication of PMMA films. A PMMA solution with a concentration of 40 mg·mL^{-1} was prepared by dissolving PMMA in chloroform under magnetic stirring. Separately, a metal precursor solution with a concentration of 8 mM was prepared by dissolving tetrachloroauric acid in chloroform under magnetic stirring. Subsequently, the PMMA and precursor solutions were mixed in a 1:1 volume ratio using an ultrasonic bath for 5 min. The films were then fabricated using the drop-casting technique, where 400 μL of the final solution, containing 20 mg·mL^{-1} of PMMA and 4 mM of precursor, was deposited onto a 1 in. diameter glass substrate on a flat surface. Finally, the samples were dried in a chloroform-rich atmosphere at room temperature for 24 h.

Moreover, the fluorescent marker rhodamine B was used to precisely determine the localization of gold nanoparticles in the PMMA polymer films after the microfabrication process. For this purpose, a 1 mM rhodamine B solution was prepared using chloroform as solvent. The fabrication of the PMMA microfilms followed the same procedure, with the final solution being prepared by mixing 198 μL of the PMMA solution, 198 μL of the precursor solution, and 4 μL of the rhodamine B solution.

2.3. Direct Laser Writing Technique. The microfabrication of the films was conducted using the experimental setup shown in Figure 1. The laser beam was collimated using a telescope before being directed toward a half-wave plate and a calcite polarizer to regulate the incident power on the sample without altering its polarization state.

Subsequently, a periscope adjusted the beam height and redirected it to a custom-built optical microscope. A 400 nm dielectric mirror guided the beam downward to a 20× microscope objective (NA = 0.6), focusing it onto the sample, which was mounted on a 3D translation stage controlled by dedicated software. A shutter was employed to control the laser beam passage onto the sample. The dielectric mirror simultaneously allowed white light (LED) transmission for sample illumination while blocking any back-reflected 405 nm light. A converging lens (10 cm focal length) projected the sample image onto a CMOS camera positioned at the microscope. All experiments were performed at room temperature in an air-saturated environment.

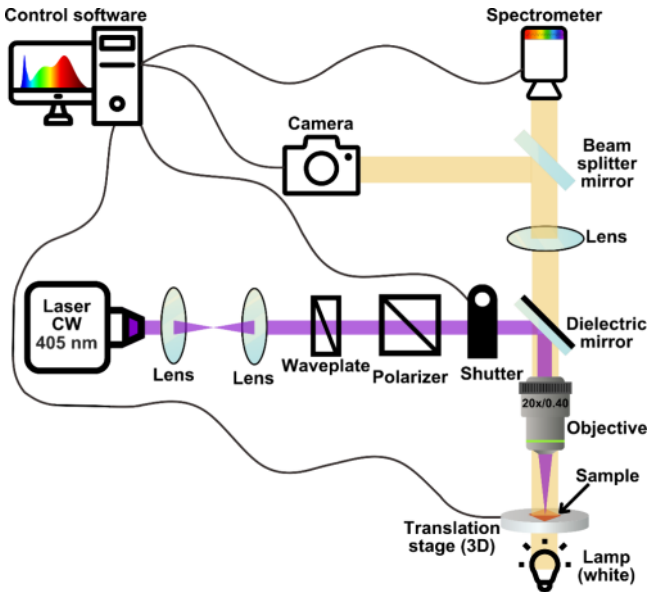

Figure 1. DLW experimental setup for microfabrication of low-cost plasmonic platforms.

A laboratory-developed software guided the fabrication of plasmonic platforms at translation speeds of 50 μm·s^{-1}, 75 μm·s^{-1}, 100 μm·s^{-1}, 200 μm·s^{-1}, 400 μm·s^{-1}, and 1000 μm·s^{-1}. Each platform featured 19 grooves, each 2 mm wide and spaced 100 μm apart. For each translation speed, platforms were created using laser powers ranging from 20 mW to 200 mW.

For the PMMA films containing both rhodamine B and gold precursor, a 100 μm·s^{-1} translation speed was used, with laser powers ranging from 20 mW to 100 mW. In this case, each platform featured nine microstructures, each 0.3 mm wide and spaced 40 μm apart.

2.4. Optical Absorption Spectroscopy. The optical absorption spectra were measured using the portable spectrometer with the same experimental setup illustrated in Figure 1. A lamp emitting from 400 to 1000 nm was positioned below the translation stage. After passing through the sample, the spectrometer collected the white light beam, which was connected to software dedicated to real-time absorption measurements. All recorded data were later analyzed using Python language. The camera allowed real-time visualization of the sample area being studied.

The images of the plasmonic platforms were captured using a camera coupled to a commercial optical microscope. For the PMMA films containing only the gold precursor, a 10×/0.25 objective lens was used, while a 40×/0.65 objective lens was employed for the films containing both the precursor and rhodamine B.

3. THEORETICAL FRAMEWORK

The Mie-Gans theory was applied to estimate the nanoparticle parameters by fitting the theoretical model to the ultraviolet-visible spectroscopy (UV−vis) experimental data.[18] The UV−vis data were collected as described in Section 2.4. Python-based software was used to apply the Mie-Gans model to the measured absorption spectra through an iterative curve-fitting procedure based on Nelder−Mead optimization. The

https://doi.org/10.1021/acsanm.5c00832
ACS Appl. Nano Mater. 2025, 8, 8294−8306

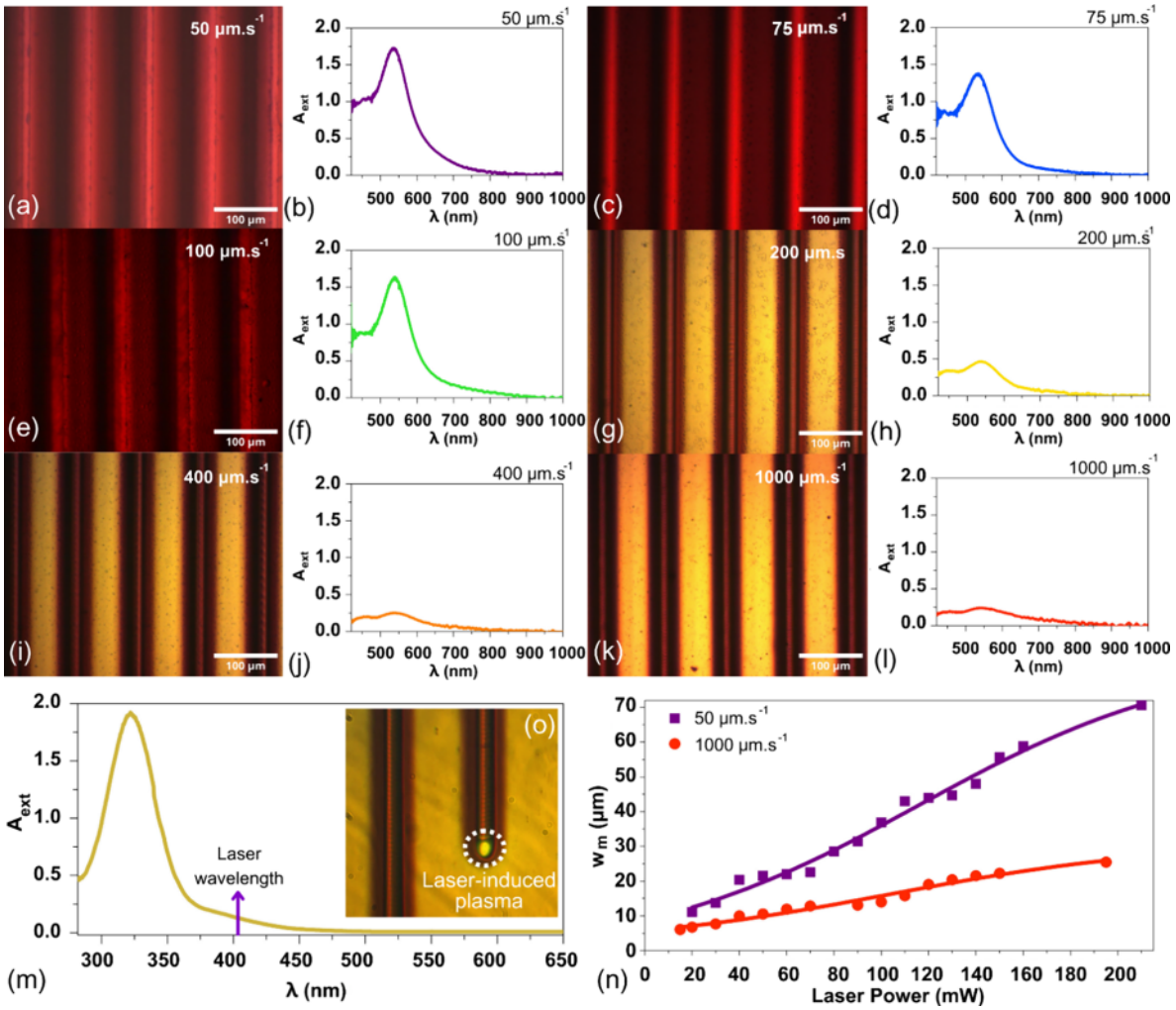

Figure 2. Optical microscopic images of the plasmonic platforms fabricated using a laser power of 150 mW and translation speeds of (a) 50 μm·s^{-1}, (c) 75 μm·s^{-1}, (e) 100 μm·s^{-1}, (g) 200 μm·s^{-1}, (i) 400 μm·s^{-1}, and (k) 1000 μm·s^{-1}. In these images, red indicates the formation of AuNPs, while yellow represents the PMMA film containing the $HAuCl_4$ precursor. The images were saturated in red to improve the visualization of the microstructures. Extinction spectra of the fabricated plasmonic platforms for translation speeds of (b) 50 μm·s^{-1}, (d) 75 μm·s^{-1}, (f) 100 μm·s^{-1}, (h) 200 μm·s^{-1}, (j) 400 μm·s^{-1}, and (l) 1000 μm·s^{-1}. (m) Absorption of the PMMA film containing the precursor before microfabrication. (n) Microstructure width (w_m, μm) as a function of the laser power (mW) for translation speeds of 50 μm·s^{-1} (violet squares) and 1000 μm·s^{-1} (red circles). (o) Real-time DLW process image for 150 mW and 200 μm·s^{-1}, highlighting the formation of laser-induced plasma.

extinction cross-section in the Mie-Gans model is outlined in eq 1, where $V = \frac{4}{3}\pi ab^2$ represents the volume of the spheroid with major and minor semiaxes b and a, respectively, $\varepsilon_m(\omega)$ denotes the dielectric constant dispersion of the surrounding medium (PMMA), λ is the wavelength of the incident photons, and $\varepsilon(\omega, R)$ is the complex dielectric function of the nanoparticle with an equivalent spherical radius $R = R_{eq} = \sqrt[3]{ab^2}$. The other parameters such as longitudinal (P_a) and transverse (P_b) depolarization and the eccentricity (e) can be found in refs 18 and 19.

$$\sigma_{ext}(\omega, R) = \frac{2\pi V \varepsilon_m^{3/2}(\omega)}{3\lambda} \sum_{j=a,b} \frac{\frac{1}{P_j^2} Im[\varepsilon(\omega, R)]}{(Re[\varepsilon(\omega, R)] + \frac{1-P_j}{P_j}\varepsilon_m)^2 + (Im[\varepsilon(\omega, R)])^2} \quad (1)$$

The complex dielectric function for metallic nanoparticles can be calculated according to eq 2, where ε_{IB} denotes the contribution of d-sp interband transitions involving bound electrons, and the term in brackets accounts for the contribution of free electrons, as described by the Drude model. Furthermore, ω_p represents the bulk plasma frequency (rad·s^{-1}), and $\omega = \frac{2\pi c}{\lambda}$ corresponds to the angular frequency of the incident light in vacuum (rad·s^{-1}), with λ being the wavelength and c the speed of light in vacuum.[55]

$$\varepsilon(\omega, R) = \varepsilon_{IB}(\omega) + [1 - \frac{\omega_p^2}{\omega(\omega + i\Gamma(R))}] \quad (2)$$

The overall damping frequency of the free electrons is size-dependent ($\Gamma(R)$) and is treated using the phenomenological approach described by Andalib et al.[55] As follows, ε_{IB} can be estimated by subtracting the contribution of the Drude model from the experimental dielectric function, as shown in eq 3.[55] In this analysis, the experimental dielectric data provided by Yakubovsky et al. was used.[56]

https://doi.org/10.1021/acsanm.5c00832
ACS Appl. Nano Mater. 2025, 8, 8294−8306

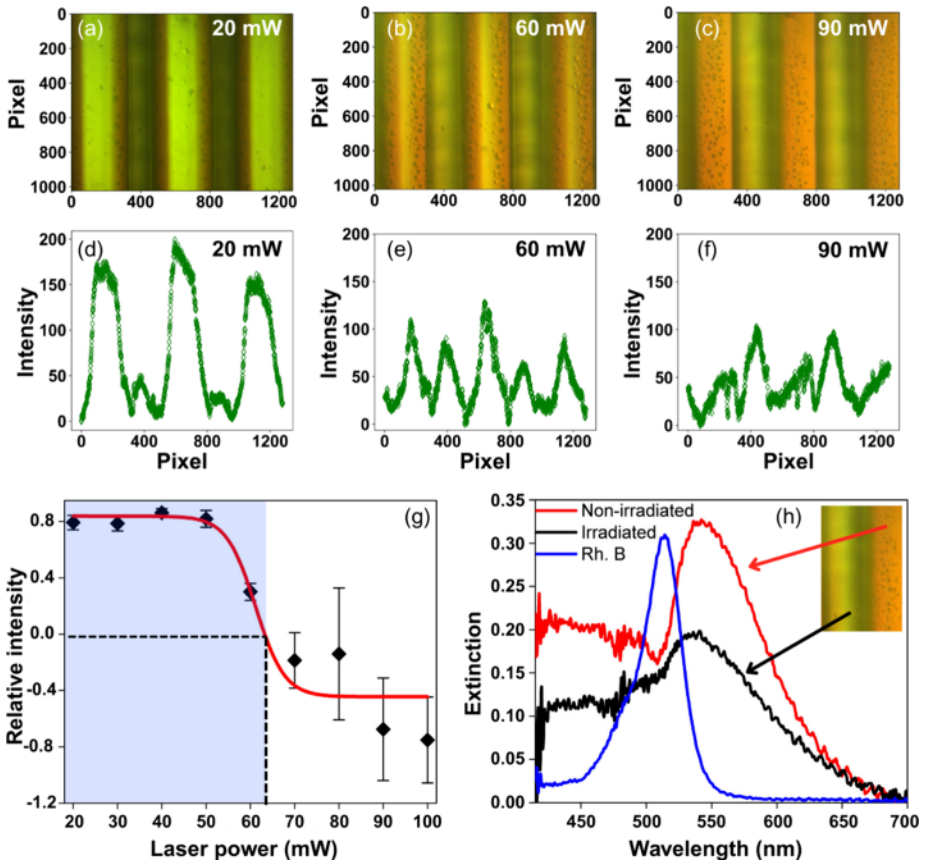

Figure 3. Optical microscopy images of the PMMA films containing the gold precursor, gold nanoparticles, and rhodamine B for a translation speed of 100 μm·s^{-1} and laser powers of (a) 20 mW, (b) 60 mW, and (c) 90 mW. Fluorescence intensity profiles were analyzed by a Python program for the same translation speed and laser powers: (d) 20 mW, (e) 60 mW, and (f) 90 mW. (g) Relative normalized intensity as a function of the laser power from 20 to 100 mW, with the blue area highlighting the transition to a high-power excitation regime (>63 mW) where most nanoparticles are concentrated outside the microstructures. (h) Extinction spectra for the center (black line) and edges (red line) of a single microstructure in the 90 mW sample, along with the extinction spectrum of rhodamine B (blue line) for the same sample.

$$\varepsilon_{IB}(\omega) = \varepsilon_{measured} - [1 - \frac{\omega_P^2}{\omega(\omega + i\Gamma(R \to \infty))}] \quad (3)$$

Accordingly, an iterative curve-fitting procedure utilizing Nelder–Mead optimization was employed in the numerical analysis of the measured optical extinction spectra via eqs 1 – 3.[18] As the initial input parameter, the nanoparticle size was estimated using an empirical formula proposed by Haiss et al.,[57] in which the radius (R) is expressed in terms of the surface plasmon resonance (A_{SPR}) and bulk gold (A_{450}) absorbance, i.e., in $R = \frac{1}{2}\exp\left[3\left(\frac{A_{SPR}}{A_{450}}\right) - 2.2\right]$.

The iterative calculation procedure, which is both fast (takes less than 1 min) and user-friendly, was executed using Python. Through the Mie-Gans fitting, the major (b) and minor (a) semiaxes of the nanoparticle were determined. Consequently, the equivalent sphere radius was calculated as the geometrical mean of the spheroid semiaxes ($R_{eq} = \sqrt[3]{ab^2}$), and the aspect ratio (shape anisotropy parameter) was defined as $\beta = b/a$.

To calculate the concentration of gold nanoparticles (AuNPs),[18,19] we employed the Beer–Lambert law in the form $[AuNP] = \frac{A_{SPR}}{\varepsilon L} = \frac{A_{SPR}}{(\sigma_{ext}\frac{N_A 10^{-3}}{\ln(10)})L}$, in which [AuNP] represents the AuNP concentration (M), A is the absorbance (measured at the SPR band maximum), L is the optical path length (cm), ε is the molar absorptivity ($M^{-1}\cdot cm^{-1}$), and N_A is the Avogadro's constant. In this context, the molar absorptivity (ε, $M^{-1}\cdot cm^{-1}$) is converted into the Mie-Gans cross section (σ_{ext}, cm^2) using a suitable correction factor.[18] Subsequently, the AuNP density (ρ, g·cm^{-3}) was estimated using $\rho = 19.3\,g\cdot cm^{-3}\frac{[AuNP]_{450}}{[AuNP]_{SPR}}$,[18] where $[AuNP]_{SPR}$ and $[AuNP]_{450}$ respectively represent the concentration of gold nanoparticles calculated at the SPR peak wavelength and 450 nm, and 19.3 g·cm^{-3} corresponds to the bulk gold density. More details about the model can be obtained from refs.[18,19]

4. RESULTS AND DISCUSSION

Figure 2a,c,e,g,i,k show optical microscopy images of the plasmonic microstructures fabricated via cw-laser direct writing on PMMA films containing $HAuCl_4$ as a precursor. The optical profilometry estimated the PMMA film thickness at (20 ± 2) μm. The yellow regions represent the PMMA film with the precursor, while the red areas indicate the formation of gold nanoparticles (AuNPs). These plasmonic microstructures were created using a laser power of 150 mW and translation speeds of 50 μm·s^{-1}, 75 μm·s^{-1}, 100 μm·s^{-1}, 200 μm·s^{-1}, 400 μm·s^{-1}, and 1000 μm·s^{-1}. As observed, the microstructure width (w_m) decreases as the translation speed increases. Lower translation speeds tend to produce larger widths due to the higher laser effective fluence ($F_{eff} = P/(vw_0)$, where P is the laser power, v is

https://doi.org/10.1021/acsanm.5c00832
ACS Appl. Nano Mater. 2025, 8, 8294–8306

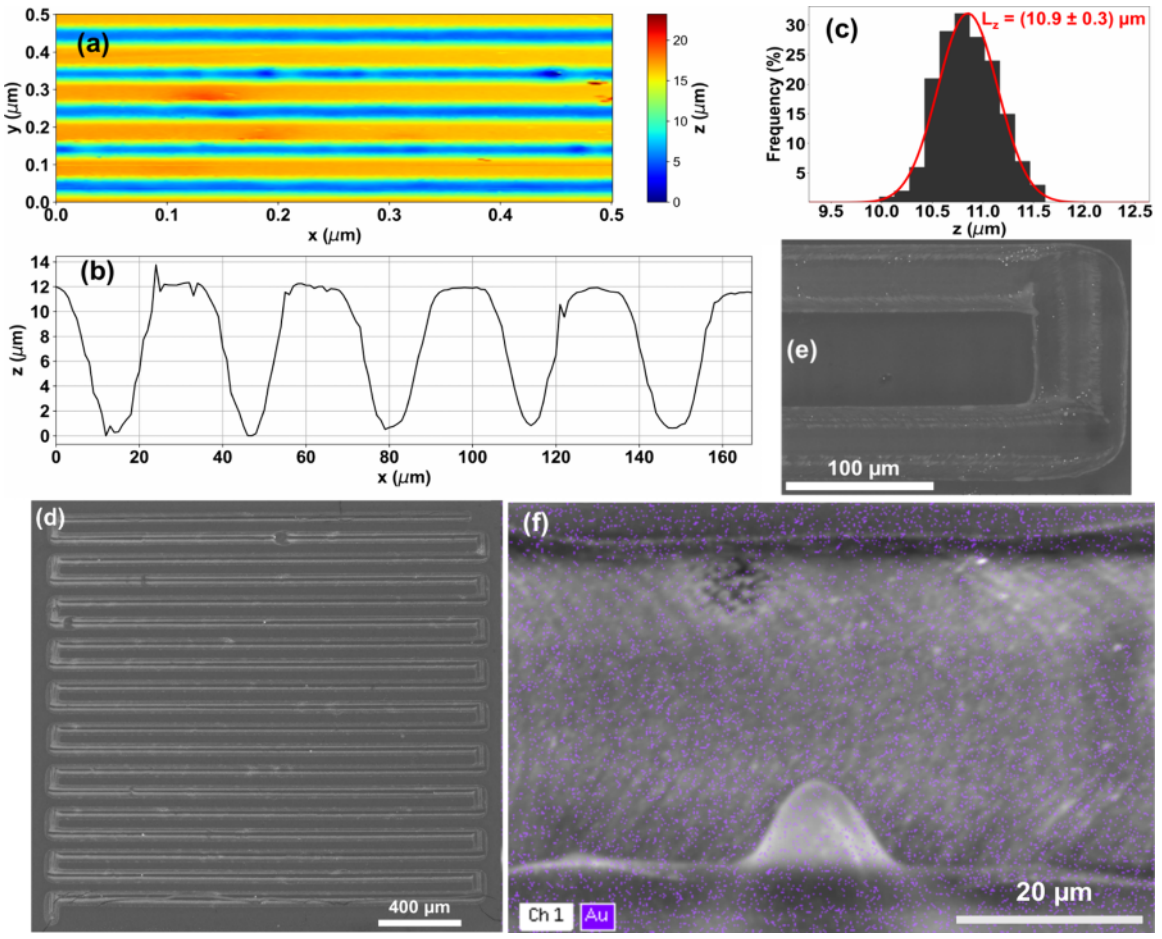

Figure 4. Optical profilometry results for the fabricated plasmonic microstructures: (a) 2D map of the surface topography, (b) cross-sectional profile, and (c) depth distribution histogram of the microstructure, showing the statistical distribution of measured depths. SEM images of the plasmonic platform: (d) overview of the entire plasmonic platform, (e) high-magnification image of a single microstructure, and (f) elemental mapping of gold (Au) distribution along a microstructure.

the translation speed, and w_0 is the beam waist radius), which increases the formation of free electron density, thus leading to higher consumption of the $HAuCl_4$ precursor. Consequently, more AuNPs are generated and higher plasma diffusion occurs, forming larger plasmonic microstructures. In summary, the $HAuCl_4$ precursor absorbs the photon at 405 nm and generates heat, which is responsible for triggering the AuNPs formation. To explain the AuNPs generation in PMMA via cw-laser, we applied the finite-difference method to solve the classical Fourier heat equation and estimate the laser-induced temperature in the PMMA/$HAuCl_4$ film. The theoretical approach and the outcomes can be observed in detail in Figure S1 from the Supporting Information. The laser-induced temperature (T_L) for a laser power of 100 mW and a laser waist radius of 3 μm reaches a very high value, T_L = 2700 K (see Figure S1 from the Supporting Information), which is much higher than the photothermal degradation temperature of PMMA (T_d = 500−700 K) even though in general the numerical simulation overestimates the temperature value due to some approximations. Consequently, in this regime, the laser-induced temperature promotes the scission of the PMMA chain, releasing volatile fragments such as CO_2 and hydrocarbons in an air-saturable atmosphere.[58] These gases form a plume near the laser focus, which has a very high irradiance of order of $GW{\cdot}m^{-2}$. Thus, the hot gas plume absorbs additional photons (stepwise multiphoton absorption) and consequently ionizes to form a "weak" plasma. In this high-temperature regime, the $HAuCl_4$ precursor decomposes directly in elemental gold (Au^0), HCl and Cl_2 or chlorine atoms as side products, forming the first gold cluster. Subsequently, with the onset of the formation of the first gold clusters, the laser-induced temperature increases considerably because of their high photothermal efficiency and large absorption cross section as compared to the $HAuCl_4$ precursor.[59−61] In this context, the laser-induced temperature can trigger a dense plasma formation, in which the NPs growth rate is accelerated through the coalescence of seed clusters, as shown in refs 43 and 44. The laser-induced plasma formation during the DLW experiments can be visualized in Figure 2o.

Figure 2b,d,f,h,j,l present the extinction spectra of the fabricated plasmonic microstructures corresponding to the optical microscopy images shown in Figure 2a,c,e,g,i,k. Notably, all extinction spectra exhibit a plasmon band around 533 nm, indicating the formation of AuNPs with spheroidal shape. Moreover, the shape of the SPR spectra without any shoulder indicates that AuNP aggregates in PMMA films are not formed via direct laser writing.[62] This outcome is interesting because it suggests that the PMMA avoids the aggregation process by acting as a surface ligand around the NPs analogously to the stabilizing molecules used in the colloidal synthesis of solution-grown NPs.[18]

https://doi.org/10.1021/acsanm.5c00832
ACS Appl. Nano Mater. 2025, 8, 8294−8306

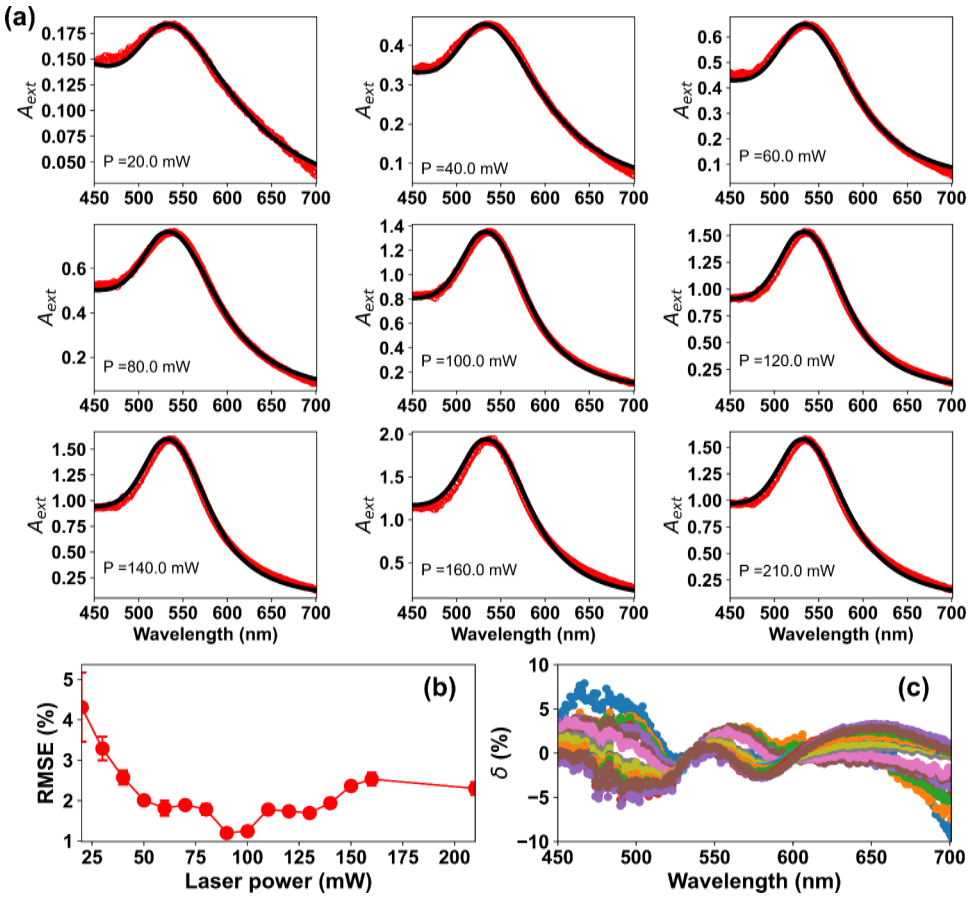

Figure 5. (a) Theoretical fits (black lines) to the experimental absorption spectra (red dots) for different laser powers, with a precursor concentration of 4 mM and a translation speed of 50 μm·s^{-1}; (b) range-normalized root mean square error (RMSE) for each laser power; (c) range-normalized deviation (δ) for each wavelength.

Figure 2m shows the absorption spectrum of the polymer film containing the precursor before microfabrication, with a band centered at 320 nm related to the $AuCl_4^-$ ion. The arrow in Figure 2m indicates the laser excitation wavelength, emphasizing the one-photon absorption-induced process related to the precursor absorption. Lastly, Figure 2n illustrates the microstructure width (μm) as a function of laser power (mW) for translation speeds of 50 μm·s^{-1} and 1000 μm·s^{-1}, with similar behavior observed for other translation speeds. Our results demonstrate that the plasmonic microstructure width can be experimentally controlled within the range of 5 to 70 μm by adjusting only the laser power and translation speed. Furthermore, reducing the plasmonic microstructure width to approximately 1 μm is possible by reducing the precursor concentration dispersed in the polymer matrix and changing the microscope objective.

To determine whether the nanoparticles were generated within the microstructure or expelled outward, we performed a fluorescence microscopy analysis by doping the PMMA films with rhodamine B. Figure 3 presents the fluorescence microscopy images (a, b, c) and the pixel intensity (d, e, f) corresponding to the fluorescence of rhodamine B for a translation speed of 100 μm·s^{-1} and laser powers of 20 mW, 60 mW, and 90 mW. In Figure 3a,d, for a laser power of 20 mW, strong fluorescence is observed outside the plasmonic microstructure, with minimal fluorescence inside, indicating that AuNPs were generated within the microstructure. Interestingly, for 60 mW (Figure 3b,e), the fluorescence intensity increased within microstructure regions and decreased in the areas between them, with a red-edge zone along the microstructures. This is likely due to the spread of nanoparticles from the microstructure with increasing laser power. In Figure 3c,f, for 90 mW, the fluorescence peaks in the microstructure regions reached their maximum, suggesting a lower concentration of AuNPs in these areas, further supporting the nanoparticle spread effect at higher laser powers. To verify the spread effect, we measured the extinction spectra for the irradiated region of a single microstructure and its nonirradiated red-edge zones in the 90 mW sample, as shown in Figure 3h. In both cases, the peak observed around 530−550 nm corresponds to the LSPR of the AuNPs. However, the LSPR intensity is higher in the edge zone (red line), indicating a greater concentration of AuNPs outside the microstructure due to the spread effect, corroborating the fluorescence microscopy measurements. To distinguish the emission of rhodamine B (Rh.B), its extinction spectrum is presented as a blue line, exhibiting a peak around 510 nm.

To better understand the spread effect, Figure 3g shows the normalized relative intensity (maximum fluorescence intensity inside the microstructures (I_i) minus the maximum intensity (I_o) between them divided by fluorescence intensity inside the microstructures, i.e., $I_R = ((I_i - I_o)/I_i)$) as a function of the laser power, ranging from 20 mW to 100 mW, for a translation speed of 100 μm·s^{-1}. A transition behavior is visible from the low-power regime (highlighted in blue) to the high-power regime (white region) as the concentration of AuNPs increases

https://doi.org/10.1021/acsanm.5c00832
ACS Appl. Nano Mater. 2025, 8, 8294−8306

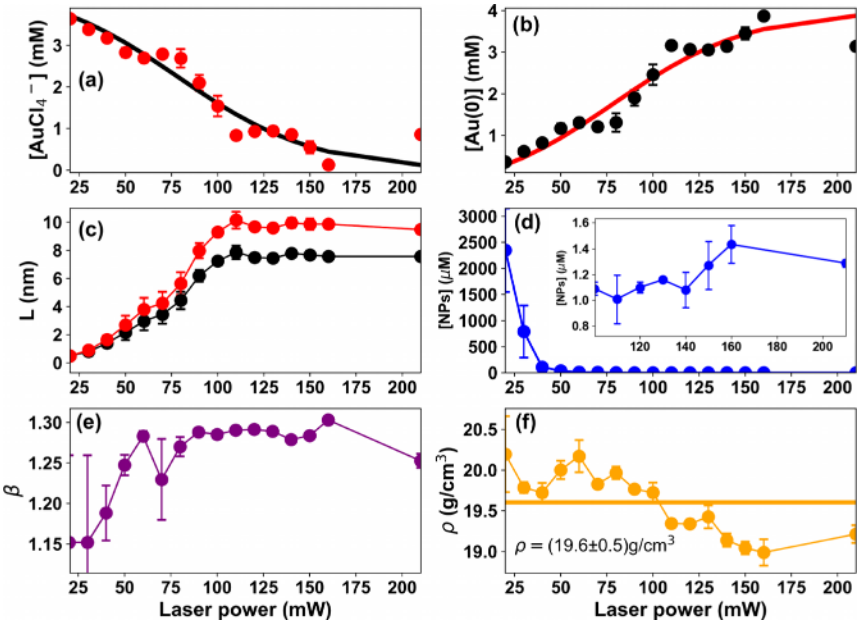

Figure 6. Physicochemical parameters describing the synthesis of AuNPs in plasmonic microstructures fabricated via direct laser writing with a 50 $\mu m \cdot s^{-1}$ translation speed and different laser powers (25−200 mW): (a) concentration of the precursor anion tetrachloroaurate ($AuCl_4^-$), (b) concentration of the generated neutral gold atoms (Au^0), (c) major (red circles) and minor (black circles) semiaxes of the spheroidal AuNPs, (d) concentration, (e) aspect ratio (β), and (f) density of the synthesized AuNPs as functions of the laser power. The solid lines in panels (a) and (b) are only an eyeguide.

outside the microstructures by raising the laser power. A tipping point occurs around 63 mW, above which more nanoparticles are found outside the microstructures due to the spread effect induced by higher laser powers.

An optical profilometry analysis was performed to gain a more comprehensive understanding of the plasmonic microstructures microfabricated, as depicted in Figure 4. Figure 4a illustrates a surface topographic map of plasmonic microstructures fabricated using laser power of 100 mW and translation speed of 200 $\mu m \cdot s^{-1}$, where the color scale represents variations in topography (z-axis). The blue color in the colormap corresponds to the groove regions of the sample, effectively highlighting the areas where the laser was focused. The groove depth depends on the laser power.

Furthermore, Figure 4b shows the cross-sectional profile along the y-axis, indicating the groove depth and shape in the geometry of the microstructures and enhancing the overall understanding of their structural characteristics. Figure 4c presents a histogram depicting the groove depth distribution of the microstructures, illustrating the frequency of different depth values. The Gaussian fit (red curve) emphasizes the average groove depth and its low dispersion, i.e., $L_z = (10.9 \pm 0.3)$ μm. Such groove depth depends on the laser irradiance. Figure 4d provides a Scanning Electron Microscopy (SEM) image of the entire plasmonic platform, which is composed of 19 individual microstructures. Each microstructure has a length of 2 mm, and the microstructures are spaced 100 μm apart. This wide-scale view offers insight into the overall arrangement and spatial configuration of the fabricated plasmonic microstructures. Figure 4e shows a high-magnification image of a single microstructure, which complements the surface analysis previously conducted through profilometry. This zoomed-in view highlights distinct grooves within the microstructure, which are most likely a result of the laser irradiation process. Lastly, Figure 4f presents the elemental mapping (energy dispersion spectroscopy) of the gold distribution across the microstructure. This image confirms the uniform presence of gold throughout the entire sample, supporting the effectiveness of the film fabrication method.

After successfully fabricating the plasmonic microstructures, a deeper analysis of the physicochemical properties of the AuNPs generated within them is required. This analysis is crucial because the optoelectronic features of plasmonic microstructures are highly dependent on the intrinsic properties of the *in situ* laser-induced AuNPs, such as nanoparticle size, concentration, density, and shape anisotropy. In previous studies,[18,19,55] we have shown that a computational approach based on the Mie-Gans model successfully describes the physicochemical properties of gold and silver nanoparticles, which were corroborated by TEM and energy-dispersive spectroscopy measurements. A very similar model was also used in ref 55 with great success in describing the growth kinetics of AuNPs synthesized via a seed-mediated chemical route. In this context, Figure 5a presents the extinction spectra of the PMMA thin films containing AuNPs, which were fabricated using a translation speed of 50 $\mu m \cdot s^{-1}$, combined with different laser powers, and a precursor concentration of 4 mM. The red circles represent the experimental data, while the solid black lines correspond to the Mie-Gans theoretical fitting curves.[18] It is worth mentioning that the plasmon band for AuNPs in PMMA is red-shifted around 13 nm compared to that in water for the same AuNP size (see Figure S2a from the Supporting Information). This shift is expected because the plasmon resonance condition should satisfy the relation $Re\{\varepsilon(\omega, R)\} = -2\varepsilon_m(\omega)$, being the dielectric constant of PMMA ($\varepsilon_m = n^2 = 2.25$, where n is the refractive index) considerably higher than that of water ($\varepsilon_m = n^2 = 1.77$), which is taken into consideration in our model (refractive index dispersion). Figure S2b confirms that the redshift is solely due

https://doi.org/10.1021/acsanm.5c00832
ACS Appl. Nano Mater. 2025, 8, 8294−8306

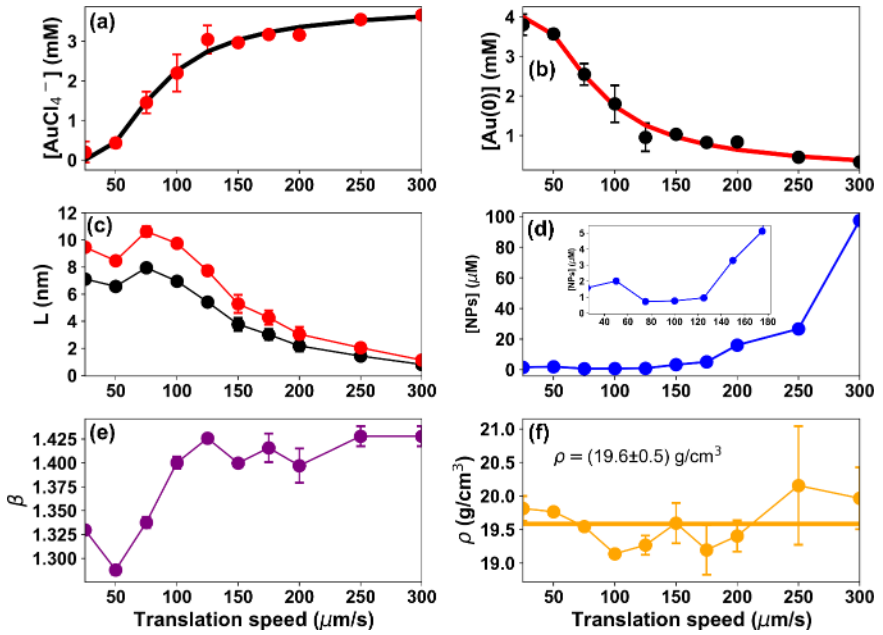

Figure 7. Physicochemical parameters describing the synthesis of AuNPs in plasmonic microstructures fabricated via direct laser writing with a 100 mW laser power and translation speed ranging from 25 to 300 $\mu m \cdot s^{-1}$: (a) concentration of the precursor anion tetrachloroaurate ($AuCl_4^-$), (b) concentration of the generated neutral gold atoms (Au^0), (c) major (red circles) and minor (black circles) semiaxes of the spheroidal AuNPs, (d) concentration, (e) aspect ratio (β), and (f) density of the synthesized AuNPs as functions of the laser power. The solid lines in panels (a) and (b) are only an eyeguide.

to the environmental medium effect and not the size of the AuNPs.

All samples exhibited a localized surface plasmon resonance (LSPR) band centered around 533 nm, characteristic of spheroidal gold nanoparticles.[18,63,64] The absorption at 450 nm is attributed to the d-sp interband transition in bulk gold, an interesting parameter for describing the properties of colloidal AuNPs.[57] To assess the accuracy of the theoretical fits of the extinction coefficient curves, we calculated the range-normalized Root Mean Square Error $\mathrm{RMSE} = \frac{\sqrt{\frac{1}{n}\sum_i^n (A_{\mathrm{exp}}^i - A_{\mathrm{theo}}^i)^2}}{(A_{\mathrm{theo}}^{\max} - A_{\mathrm{theo}}^{\min})}$, where A_{theo}^{max} and A_{theo}^{min} are the maximum and minimum values of the theoretical extinction coefficient, respectively. The RMSE for each extinction coefficient curve obtained with different laser powers is shown in Figure 5b. Additionally, we calculated the range-normalized deviation $\delta(\lambda) = 100[\frac{|A_{\mathrm{exp}}(\lambda) - A_{\mathrm{theo}}(\lambda)|}{(A_{\mathrm{theo}}^{\max} - A_{\mathrm{theo}}^{\min})}]$. This parameter represents the deviation between experimental data and theoretical fits at each wavelength, as shown in Figure 5c. These metrics demonstrate the high reliability of the numerical fitting model, with a confidence interval of approximately 95%.[55] Therefore, this model accurately reproduces all measured extinction spectra, allowing us to extract information about the colloidal AuNPs synthesized within the plasmonic microstructures. For instance, Figure 6 illustrates various physicochemical parameters estimated from the Mie-Gans-based theoretical framework described in Section 3: the consumption of $HAuCl_4$ precursor (Figure 6a), the formation of Au^0 (neutral gold) atoms (Figure 6b), the major and minor semiaxes of the gold nanoparticles (Figure 6c), their concentration (Figure 6d), shape anisotropy (Figure 6e), and density (Figure 6f) as functions of the laser power during the fabrication of the plasmonic microstructure via direct laser writing using a 50 $\mu m \cdot s^{-1}$ translation speed.

Figure 6a illustrates that progressively higher laser powers lead to an increasingly pronounced consumption of the $HAuCl_4$ precursor because the laser-generated plasma density becomes greater, forming more neutral gold atoms and consequently more clusters. This process contributes to the nucleation and growth of AuNPs. Indeed, the formation of AuNPs via DLW is driven by PMMA photothermal degradation followed by laser-induced plasma, initiating the PMMA chain scission.[65] As mentioned, these photophysical events generate zerovalent Au atoms, which then aggregate into nuclei and subsequently grow. Notably, it is worth mentioning that this growth process ceases immediately after laser irradiation, unlike the traditional AuNP formation in solution, where growth via incorporation of neutral gold atoms continues even without excitation until the remaining metal precursor molecules are completely depleted. Therefore, this synthesis method is more controllable in a PMMA polymer matrix than in a solution containing suitable chemical precursors.

Figures 6c,d show the major (red dots) and minor (black dots) semiaxes (characteristic particle sizes for the spheroidal shape) and the concentration of AuNPs, respectively. Initially, nanoparticles with very small sizes are generated at high concentrations (1.9 mM) due to the low laser power and the resulting small Au^0 atom density within the PMMA matrix. As the laser power increases, the AuNPs grow while their concentration decreases rapidly up to a laser power of 110 mW. Beyond this point, the AuNP size stabilizes, the growth curve reaches an almost constant level, while the nanoparticle concentration increases (inset of Figure 6d) because the $AuCl_4^-$ precursor anion remains available for further consumption, as indicated in Figure 6a.

Finally, Figure 6e,f present the shape anisotropy parameter (aspect ratio of the spheroidal nanoparticle) and the density of AuNPs generated via the DLW technique, respectively.

https://doi.org/10.1021/acsanm.5c00832
ACS Appl. Nano Mater. 2025, 8, 8294−8306

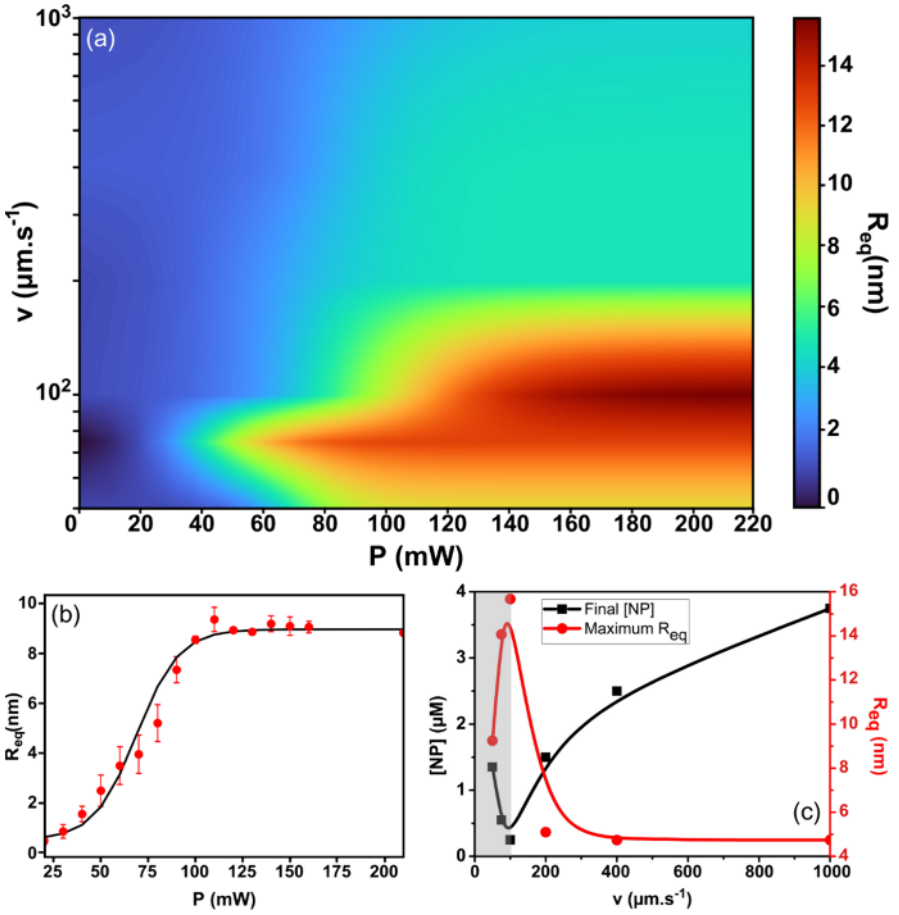

Figure 8. (a) Colormap for the equivalent spherical radius (R_{eq}; nm) as a function of laser power (P; mW) and translation speed (v; μm·s^{-1}); (b) R_{eq} as a function of laser power (P) for gold nanoparticles synthesized using a translation speed of 50 μm·s^{-1}; (c) final nanoparticle concentration ([NP], black squares; μM) and maximum R_{eq} (red circles; nm) as functions of translation speed (v; μm·s^{-1}), where the inserted lines serve as visual guides to highlight the trends observed in the samples.

Initially, due to the low density of free electrons induced by the low laser fluence, ultrasmall AuNPs with large surface area are produced. Consequently, AuNPs with approximately spherical shapes are produced, i.e., low anisotropy ($\beta \sim 1.2$).[55]

In this scenario, the number of laser-generated Au^0 atoms is very small, which prevents the growth stage from proceeding after nucleation due to the lack of Au^0 atoms available in the irradiated PMMA film. Consequently, this process affects the structural quality of AuNPs, resulting in higher nanoparticle density. As the laser power increases, more Au^0 atoms are generated, allowing the growth stage to proceed, thus increasing the size of the AuNPs. This also leads to a rise in anisotropy due to the larger concentration of available Au^0 atoms or even due to the coalescence of seed clusters.[66,67] As a result, there is a reduction in AuNP density, approaching the bulk gold value (19.3 g·cm^{-3}) due to the improved structural quality of the nanoparticles. These analyses can be similarly applied to AuNP samples in PMMA plasmonic platforms fabricated with different translation speeds.

Similar analyses were then conducted on AuNP samples synthesized in a PMMA film with the laser power fixed at 100 mW and the translation speed varying from 25 μm·s^{-1} to 300 μm·s^{-1}, as illustrated in Figure 7. Figure 7a shows the consumption of $HAuCl_4$ precursor as a function of the translation speed, while Figure 7b displays the corresponding formation of Au^0 atoms. In contrast to the effects of laser power exhibited in Figure 6a,b, lower translation speeds result in increased precursor consumption due to the higher laser effective fluence, which enhances electron generation and, consequently, the formation of Au^0 atoms and their subsequent agglomeration into nuclei and AuNPs. Figure 7c depicts the major and minor semiaxes of the AuNPs, and Figure 7d shows their concentration. Notably, there is a maximum AuNP size and a corresponding minimum AuNP concentration at a translation speed between 75 and 100 μm·s^{-1}. As the translation speed increases beyond this point, there is a reduction in the AuNPs size and an increase in their concentration because of the short time of laser interaction with the sample. Such interaction time can be calculated as $t_{int} = 2w_0/v$.

The shape anisotropy factor (particle aspect ratio) is shown in Figure 7e, where it is evident that there is no significant change in its value for translation speeds above 100 μm·s^{-1}. However, the anisotropy decreases for speeds below 100 μm·s^{-1}. The described behavior change is likely due to the laser-induced particle fragmentation process[68] for translation speeds greater than ~75 μm·s^{-1} combined with high laser power (100 mW, very high fluence laser), which is corroborated by the observed AuNP size reduction (see Figure 7c) accompanied by the AuNP concentration increase (see Figure 7d). Such reshaping/fragmentation process can be explained because once larger AuNPs are generated the laser-induced temper-

https://doi.org/10.1021/acsanm.5c00832
ACS Appl. Nano Mater. 2025, 8, 8294−8306

ature increases dramatically, triggering these effects. In particular, the laser-induced temperature is directly proportional to the absorbed laser power (P_{abs}) that depends on the extinction cross-section (σ_{ext}), the latter of which scales with the cube of the NP radius ($T \infty P_{abs} \propto \sigma_{ext} \propto R_{eq}^3$).[69] Therefore, small increases in NP radius cause a large increase in laser-induced temperature. Figure 7f shows the density of the nanoparticles, which exhibit minimal variations. The average value is 19.7 ± 0.5 g·cm^{-3}, indicating the production of high-quality AuNPs.

Figure 7a,b show that the consumption of $HAuCl_4$ precursor and the formation of Au^0 atoms follow a sigmoidal behavior as a function of translation speed or interaction time (Figure S3 from the Supporting Information) (t_{int} from 0.02 s (v = 300 μm·s^{-1}) to 0.24 s (v = 25 μm·s^{-1})). This sigmoidal behavior suggests that the AuNPs growth in PMMA may be described by a rapid autocatalytic growth stage.[70] As observed in Figure S3, the growth rate is very high, i.e., the growth stage practically finishes at around 100 ms, which corroborates with the dense plasma formation after the generation of the first gold clusters.

Figure 8a presents a colormap for the equivalent-sphere radius $R_{eq} = \sqrt[3]{ab^2}$ (geometrical average of the spheroidal AuNP semiaxes a and b) as a function of laser power (P; mW) and translation speed (v; μm·s^{-1}). The colormap was generated through a curve fitting procedure using a sigmoidal function implemented via Python, as represented by the solid line in Figure 8b. Moreover, we applied the interpolation method to obtain information about the R_{eq} values corresponding to additional translation speeds inserted between 50 μm·s^{-1} and 1000 μm·s^{-1} to generate a smoothed colormap. Figure 8b illustrates R_{eq} as a function of laser power P for a fixed speed of 50 μm·s^{-1}, revealing a clear sigmoidal behavior that remains consistent across all translation speeds. According to this model, spheroidal AuNPs with equivalent spherical diameters ranging from 2 to approximately 30 nm can be synthesized by adjusting laser power and speed. Interestingly, our data present optimal translation speed (100 μm·s^{-1}) and laser power (100 mW) for AuNP microfabrication in PMMA films, facilitating the production of gold nanoparticles within a broad size range (R_{eq} = 1 to 15 nm). Contrary to expectations, larger AuNPs were not observed at lower translation speeds (e.g., 50 μm·s^{-1}); instead, a reduction in particle size was noted at speeds below 100 μm·s^{-1}, as shown in Figure 8c, which compares the maximum R_{eq} values (red circles) corresponding to different translation speeds (v). As mentioned, this reduction is likely attributed to laser-induced particle reshaping/fragmentation,[68] which is promoted by the prolonged duration of laser-induced plasma at lower translation speeds.

This hypothesis is further supported by the final nanoparticle concentration data ([NP], black squares) compiled in Figure 8c, which exhibit a trend opposite to that observed for the R_{eq} vs v curve, that is, [NP] rises substantially for v < 100 μm·s^{-1} (see the gray filled area in Figure 8c comparing the evolution of the nanoparticle size and concentration for low translation speeds). When particle fragmentation occurs, an increase in AuNP concentration is expected, which is consistent with the observed results.

5. CONCLUSIONS

We experimentally controlled the physicochemical properties of AuNPs synthesized within PMMA films containing tetrachloroauric acid using direct laser writing. By modulating only the laser power and translation speed, we achieved precise fabrication of AuNPs with tunable sizes ranging from 2 to 30 nm, shape anisotropy factors (aspect ratio) between ∼1.1 and 1.5, and concentrations spanning from 0.9 μM to 1.9 mM. These particles exhibited densities comparable to bulk gold, forming plasmonic microstructures with dimensions from 5 to 70 μm. Furthermore, rhodamine B fluorescence mapping revealed a tendency for nanoparticles to spread outside the microstructures at high laser powers, with a critical tipping point identified at approximately 63 mW, above which AuNP concentration increased significantly beyond the patterned regions. This approach demonstrates the ability to synthesize size-tunable AuNPs in PMMA plasmonic platforms with micrometer-scale precision by simply adjusting laser parameters without requiring additional control over temperature, pressure, atmosphere, or prefabrication masks. The technique offers a versatile, cost-effective alternative to conventional methods. Additionally, integrating UV−vis spectroscopy with a Mie-Gans-based computational framework enabled efficient quantitative analyses of the nanoparticles, highlighting its utility for characterizing nanostructures generated in polymers. Our findings provided new insights into the interplay between laser parameters and nanoparticle generation, advancing the field of nanomaterials science and engineering. This work paves the way for innovative applications in nanoscale research and opens up opportunities for cost-effective, high-resolution nanopatterning.

■ ASSOCIATED CONTENT

Supporting Information

The Supporting Information is available free of charge at https://pubs.acs.org/doi/10.1021/acsanm.5c00832.

The theoretical model based on the classical Fourier heat equation used to estimate the laser-induced temperature in the PMMA/$HAuCl_4$ film; comparison between the plasmon band for AuNPs in water and PMMA; physicochemical parameters describing the synthesis of AuNPs in plasmonic microstructures fabricated via direct laser writing as a function of laser interaction time (PDF)

■ AUTHOR INFORMATION

Corresponding Author

Marcelo Gonçalves Vivas − *Laboratório de Espectroscopia Óptica e Fotônica, Universidade Federal de Alfenas, Poços de Caldas, MG 37715-400, Brazil;* orcid.org/0000-0003-4777-1323; Email: mavivas82@gmail.com

Authors

Richard Silveira Pereira − *Laboratório de Espectroscopia Óptica e Fotônica, Universidade Federal de Alfenas, Poços de Caldas, MG 37715-400, Brazil;* orcid.org/0009-0004-5229-6058

Diego Lourençoni Ferreira − *Laboratório de Espectroscopia Óptica e Fotônica, Universidade Federal de Alfenas, Poços de Caldas, MG 37715-400, Brazil;* orcid.org/0000-0002-0688-1801

https://doi.org/10.1021/acsanm.5c00832
ACS Appl. Nano Mater. 2025, 8, 8294−8306

Gabriel Ferrari de Oliveira − *Laboratório de Espectroscopia Óptica e Fotônica, Universidade Federal de Alfenas, Poços de Caldas, MG 37715-400, Brazil;* orcid.org/0000-0002-1659-2974

Gabriele C. Felipe de Paula − *Instituto de Física de São Carlos, Universidade de São Paulo, São Carlos, SP 13566-590, Brazil;* orcid.org/0009-0002-1048-9260

André Luís dos Santos Romero − *Instituto de Física de São Carlos, Universidade de São Paulo, São Carlos, SP 13566-590, Brazil;* orcid.org/0000-0001-9982-8171

Cleber Renato Mendonça − *Instituto de Física de São Carlos, Universidade de São Paulo, São Carlos, SP 13566-590, Brazil;* orcid.org/0000-0001-6672-2186

Complete contact information is available at: https://pubs.acs.org/10.1021/acsanm.5c00832

Funding

The Article Processing Charge for the publication of this research was funded by the Coordenacao de Aperfeicoamento de Pessoal de Nivel Superior (CAPES), Brazil (ROR identifier: 00x0ma614).

Notes

The authors declare no competing financial interest.

■ ACKNOWLEDGMENTS

Financial support from FAPEMIG (*Fundação de Amparo à Pesquisa do Estado de Minas Gerais*, APQ-02101-23, and BPD-00434-22), FAPESP (*Fundação de Amparo à Pesquisa do Estado de São Paulo*, grants 2018/11283-7), Army Research Laboratory (W911NF2110362), Air Force Office of Scientific Research (FA9550-23-1-0664), CNPq (*Conselho Nacional de Desenvolvimento Científico e Tecnológico, 307550/2021-4*), and CAPES (*Coordenação de Aperfeiçoamento de Pessoal de Nível Superior*) is acknowledged. D.L.F. is grateful to CAPES for providing the postdoctoral fellowship granted ("*Bolsista CAPES/BRASIL*").

■ REFERENCES

(1) Ohannesian, N.; Misbah, I.; Lin, S. H.; Shih, W.-C. Plasmonic Nano-Aperture Label-Free Imaging (PANORAMA). *Nat. Commun.* **2020**, *11* (1), 5805.

(2) Zhang, P.; Zhou, X.; Jiang, J.; Kolay, J.; Wang, R.; Ma, G.; Wan, Z.; Wang, S. In Situ Analysis of Membrane-Protein Binding Kinetics and Cell−Surface Adhesion Using Plasmonic Scattering Microscopy. *Angew. Chem., Int. Ed.* **2022**, *61* (42), 134.

(3) Yang, Y.; Zhai, C.; Zeng, Q.; Khan, A. L.; Yu, H. Quantitative Amplitude and Phase Imaging with Interferometric Plasmonic Microscopy. *ACS Nano* **2019**, *13* (11), 13595−13601.

(4) Gurban, A. M.; Zamfir, L. G.; Epure, P.; Şuică-Bunghez, I. R.; Senin, R. M.; Jecu, M. L.; Jinga, M. L.; Doni, M. Flexible Miniaturized Electrochemical Sensors Based on Multiwalled Carbon Nanotube-Chitosan Nanomaterial for Determination of Nitrite in Soil Solutions. *Chemosensors* **2023**, *11* (4), 224.

(5) Song, S.; Lee, J. U.; Jeon, M. J.; Kim, S.; Sim, S. J. Detection of Multiplex Exosomal MiRNAs for Clinically Accurate Diagnosis of Alzheimer's Disease Using Label-Free Plasmonic Biosensor Based on DNA-Assembled Advanced Plasmonic Architecture. *Biosens Bioelectron* **2022**, *199*, No. 113864.

(6) Guchhait, S.; Chatterjee, S.; Chakravarty, T.; Ghosh, N. A Metal-Insulator-Metal Waveguide-Based Plasmonic Refractive Index Sensor for the Detection of Nanoplastics in Water. *Sci. Rep* **2024**, *14* (1), 21495.

(7) da Silva Rodrigues, D. C.; de Oliveira, G. F.; dos Santos Romero, A. L.; Vieira, N. C. S.; Vivas, M. G. Surface Plasmon Resonance Spectrometer in the Double Prism Configuration: Fast Characterization of the Thickness and Dielectric Constant Dispersion of Thin Films. *Sens Actuators A Phys.* **2025**, *381*, No. 116067.

(8) Yang, L.; Zhao, Z.; Tian, B.; Yang, M.; Dong, Y.; Zhou, B.; Gai, S.; Xie, Y.; Lin, J. A Singular Plasmonic-Thermoelectric Hollow Nanostructure Inducing Apoptosis and Cuproptosis for Catalytic Cancer Therapy. *Nat. Commun.* **2024**, *15* (1), 7499.

(9) Ye, Q.-N.; Zhu, L.; Liang, J.; Zhao, D.-K.; Tian, T.-Y.; Fan, Y.-N.; Ye, S.-Y.; Liu, H.; Huang, X.-Y.; Cao, Z.-T.; Shen, S.; Wang, J. Orchestrating NK and T Cells via Tri-Specific Nano-Antibodies for Synergistic Antitumor Immunity. *Nat. Commun.* **2024**, *15* (1), 6211.

(10) Duan, X.; Kamin, S.; Liu, N. Dynamic Plasmonic Colour Display. *Nat. Commun.* **2017**, *8* (1), 14606.

(11) Franklin, D.; Frank, R.; Wu, S.-T.; Chanda, D. Actively Addressed Single Pixel Full-Colour Plasmonic Display. *Nat. Commun.* **2017**, *8* (1), 15209.

(12) Liang, J.; Jin, Y.; Yu, H.; Chen, X.; Zhou, L.; Huo, P.; Zhang, Y.; Ma, H.; Jiang, Y.; Zhu, B.; Xu, T.; Liu, H.; Zhu, S.; Zhu, J. Lithium-Plasmon-Based Low-Powered Dynamic Color Display. *Natl. Sci. Rev.* **2023**, *10* (1), No. nwac120.

(13) Zhu, X.; Vannahme, C.; Højlund-Nielsen, E.; Mortensen, N. A.; Kristensen, A. Plasmonic Colour Laser Printing. *Nat. Nanotechnol.* **2016**, *11* (4), 325−329.

(14) Wu, P.-Y.; Lee, W.-Q.; Liu, C.-H.; Huang, C.-B. Coherent Control of Enhanced Second-Harmonic Generation in a Plasmonic Nanocircuit Using a Transition Metal Dichalcogenide Monolayer. *Nat. Commun.* **2024**, *15* (1), 1855.

(15) Hu, S.; Huang, J.; Arul, R.; Sánchez-Iglesias, A.; Xiong, Y.; Liz-Marzán, L. M.; Baumberg, J. J. Robust Consistent Single Quantum Dot Strong Coupling in Plasmonic Nanocavities. *Nat. Commun.* **2024**, *15* (1), 6835.

(16) Zhao, W.; Luo, L.; Cong, M.; Liu, X.; Zhang, Z.; Bahri, M.; Li, B.; Yang, J.; Yu, M.; Liu, L.; Xia, Y.; Browning, N. D.; Zhu, W.-H.; Zhang, W.; Cooper, A. I. Nanoscale Covalent Organic Frameworks for Enhanced Photocatalytic Hydrogen Production. *Nat. Commun.* **2024**, *15* (1), 6482.

(17) Hu, N.; Ding, L.; Wang, A.; Zhou, W.; Zhang, C.; Zhang, B.; Yin, R. Comprehensive Modeling of Corkscrew Motion in Micro-/Nano-Robots with General Helical Structures. *Nat. Commun.* **2024**, *15* (1), 7399.

(18) Ferreira, D. L.; Pereira, C. F. J.; Vivas, M. G. Unveiling Step-by-Step the Bottom-Up Kinetics and Growth Mechanism of Laser-Induced Colloidal Gold Nanoparticles. *J. Phys. Chem. C* **2023**, *127* (37), 18533−18546.

(19) Pacheco, P. G. F.; Ferreira, D. L.; Pereira, R. S.; Vivas, M. G. Physicochemical Properties of Ultrasmall Colloidal Silver Nanoparticles: An Experimental and Computational Approach. *Analyst* **2023**, *148* (20), 5262−5269.

(20) Yuan, H.; Ji, W.; Chu, S.; Liu, Q.; Qian, S.; Guang, J.; Wang, J.; Han, X.; Masson, J.-F.; Peng, W. Mercaptopyridine-Functionalized Gold Nanoparticles for Fiber-Optic Surface Plasmon Resonance Hg^{2+} Sensing. *ACS Sens* **2019**, *4* (3), 704−710.

(21) Yang, F.; Song, W.; Zhang, C.; Fang, H.; Min, C.; Yuan, X. A Phase-Shifted Surface Plasmon Resonance Sensor for Simultaneous Photoacoustic Volumetric Imaging and Spectroscopic Analysis. *ACS Sens* **2021**, *6* (5), 1840−1848.

(22) Ahmed, R.; Guimarães, C. F.; Wang, J.; Soto, F.; Karim, A. H.; Zhang, Z.; Reis, R. L.; Akin, D.; Paulmurugan, R.; Demirci, U. Large-Scale Functionalized Metasurface-Based SARS-CoV-2 Detection and Quantification. *ACS Nano* **2022**, *16* (10), 15946−15958.

(23) Gadelha, A. C.; Ohlberg, D. A. A.; Rabelo, C.; Neto, E. G. S.; Vasconcelos, T. L.; Campos, J. L.; Lemos, J. S.; Ornelas, V.; Miranda, D.; Nadas, R.; Santana, F. C.; Watanabe, K.; Taniguchi, T.; van Troeye, B.; Lamparski, M.; Meunier, V.; Nguyen, V.-H.; Paszko, D.; Charlier, J.-C.; Campos, L. C.; Cançado, L. G.; Medeiros-Ribeiro, G.; Jorio, A. Localization of Lattice Dynamics in Low-Angle Twisted Bilayer Graphene. *Nature* **2021**, *590* (7846), 405−409.

(24) Zhang, X.; Lei, Z.; Pan, Z.; Hu, J.; Tao, L.; Zheng, Z.; Feng, X.; Xue, J.; Tao, L.; Zhao, Y. A General Approach to Hybrid Platform of

Au Nanoparticles on Monolayer Semiconductor for Ultrasensitive Raman Enhancement of 2D Materials and Molecule Detection. *J. Alloys Compd.* **2023**, *938*, No. 168468.
(25) Doanh, T. T.; Van Hieu, N.; Quynh Trang, T. N.; Hanh Thu, V. T. In Situ Synthesis of Hybrid Zinc Oxide-Silver Nanoparticle Arrays as a Powerful Active Platform for Surface-Enhanced Raman Scattering Detection. *J. Sci.:Adv. Mater. Dev.* **2021**, *6* (3), 379−389.
(26) Kim, Y.-Y.; Bang, Y.; Lee, A.-H.; Song, Y.-K. Multivalent Traptavidin−DNA Conjugates for the Programmable Assembly of Nanostructures. *ACS Nano* **2019**, *13* (2), 1183−1194.
(27) Wu, M.; Xu, N.; Wang, E.; Gen, S.; Zhu, H.; Liu, C.; Cao, J. Nanogratings Fabricated by Wet Etching Assisted Femtosecond Laser Modification of Silicon for Surface Plasmon Resonance Sensing. *Appl. Surf. Sci.* **2022**, *603*, No. 154446.
(28) Mamykin, S. V.; Gnilitskyi, I. M.; Dusheyko, M. G.; DeVol, T. A.; Bliznyuk, V. N. Femtosecond Laser Nano-Structuring for Surface Plasmon Resonance-Based Detection of Uranium. *Appl. Surf. Sci.* **2022**, *576*, No. 151831.
(29) Al-Bataineh, Q. M.; Rjoub, G.; Telfah, A. D.; Ahmad, A. A.; Tavares, C. J.; Hergenröder, R. Developing Surface Plasmon Resonance Imaging for Discrete Particle Detection Based on a Silver Layer Coated with Polyacrylic Acid/Iodine Polyelectrolyte Brushes. *Appl. Surf. Sci.* **2025**, *682*, No. 161755.
(30) Pan, Y.; Xu, K. Recent Progress in Nano-Electronic Devices Based on EBL and IBL. *Curr. Nanosci* **2020**, *16* (2), 157−169.
(31) Bhagoria, P.; Mathew Sebastian, E.; Kumar Jain, S.; Purohit, J.; Purohit, R. Nanolithography and Its Alternate Techniques. *Mater. Today Proc.* **2020**, *26*, 3048−3053.
(32) Sebastian, E. M.; Jain, S. K.; Purohit, R.; Dhakad, S. K.; Rana, R. S. Nanolithography and Its Current Advancements. *Mater. Today Proc.* **2020**, *26*, 2351−2356.
(33) Yoon, G.; Tanaka, T.; Zentgraf, T.; Rho, J. Recent Progress on Metasurfaces: Applications and Fabrication. *J. Phys. D Appl. Phys.* **2021**, *54* (38), No. 383002.
(34) Li, M.; Chen, Y.; Luo, W.; Cheng, X. Interfacial Interactions during Demolding in Nanoimprint Lithography. *Micromachines* **2021**, *12* (4), 349.
(35) Zhang, J.; Cong, C.; Guo, C. Single-Step Maskless Nano-Lithography on Glass by Femtosecond Laser Processing. *J. Appl. Phys.* **2020**, *127* (16), No. 163102.
(36) Sharma, E.; Rathi, R.; Misharwal, J.; Sinhmar, B.; Kumari, S.; Dalal, J.; Kumar, A. Evolution in Lithography Techniques: Micro-lithography to Nanolithography. *Nanomaterials* **2022**, *12* (16), 2754.
(37) Waller, E. H.; Dix, S.; Gutsche, J.; Widera, A.; von Freymann, G. Functional Metallic Microcomponents via Liquid-Phase Multi-photon Direct Laser Writing: A Review. *Micromachines* **2019**, *10* (12), 827.
(38) Kindle, C.; Castonguay, A.; McGee, S.; Tomko, J. A.; Hopkins, P. E.; Zarzar, L. D. Direct Laser Writing from Aqueous Precursors for Nano to Microscale Topographical Control, Integration, and Synthesis of Nanocrystalline Mixed Metal Oxides. *ACS Appl. Nano Mater.* **2019**, *2* (5), 2581−2586.
(39) Srikanth, S.; Dudala, S.; Raut, S.; Dubey, S. K.; Ishii, I.; Javed, A.; Goel, S. Optimization and Characterization of Direct UV Laser Writing System for Microscale Applications. *J. Micromech. Microeng.* **2020**, *30* (9), No. 095003.
(40) Milles, S.; Soldera, M.; Kuntze, T.; Lasagni, A. F. Characterization of Self-Cleaning Properties on Superhydrophobic Aluminum Surfaces Fabricated by Direct Laser Writing and Direct Laser Interference Patterning. *Appl. Surf. Sci.* **2020**, *525*, No. 146518.
(41) Wang, S.; Yao, J.; Lu, X.; Ding, T. Light-Induced Solid-State Protrusion of Gold Nanowires and Their Derivatives for Sensing Applications. *Adv. Opt. Mater.* **2022**, *10* (6), No. 2102238.
(42) Wang, S.; Ding, T. Laser-Directed Asymmetric Growth of Plasmonic Chiral Ensembles. *Laser Photon Rev.* **2022**, *16* (10), No. 2100526.
(43) Geladari, O.; Eberle, M.; Maier, A.; Fetzer, F.; Chassé, T.; Meixner, A. J.; Scheele, M.; Schnepf, A.; Braun, K. Nanometer Sized Direct Laser-Induced Gold Printing for Precise 2D-Electronic Device Fabrication. *Small Methods* **2023**, *7* (7), No. 2201221.
(44) Geladari, O.; Haizmann, P.; Maier, A.; Strienz, M.; Eberle, M.; Scheele, M.; Peisert, H.; Schnepf, A.; Chassé, T.; Braun, K.; Meixner, A. J. Direct Laser Induced Writing of High Precision Gold Nanosphere SERS Patterns. *Nanoscale Adv.* **2024**, *6* (4), 1213−1217.
(45) Du, Y.; Pei, P.; Suo, T.; Gao, G. Large Deformation Mechanical Behavior and Constitutive Modeling of Oriented PMMA. *Int. J. Mech Sci.* **2023**, *257*, No. 108520.
(46) Zayed, M. E. M.; Obaid, A. Y.; Almulaiky, Y. Q.; El-Shishtawy, R. M. Enhancing the Sustainable Immobilization of Laccase by Amino-Functionalized PMMA-Reinforced Graphene Nanomaterial. *J. Environ. Manage* **2024**, *351*, No. 119503.
(47) Zhao, X.; Gao, J.; Han, H.; Lou, X.; Ma, H.; Su, X.; Zhang, L.; Tian, J.; Lei, B.; Zhang, Y. Bioactive Strong Biodegradable Bone Cement for Rapid Osteointegration and Osteogenesis. *Chem. Eng. J.* **2023**, *474*, No. 145609.
(48) Abed, R. N.; Zainulabdeen, K.; Abdallh, M.; Yousif, E.; Rashad, A. A.; Jawad, A. H. The Optical Properties Behavior of Modify Poly(Methyl Methacrylate) Nanocomposite Thin Films during Solar Energy Absorption. *J. Non Cryst. Solids* **2023**, *609*, No. 122257.
(49) Bakr, A. M.; Darwish, A.; Azab, A. A.; El Awady, M. E.; Hamed, A. A.; Elzwawy, A. Structural, Dielectric, and Antimicrobial Evaluation of PMMA/CeO2 for Optoelectronic Devices. *Sci. Rep* **2024**, *14* (1), 2548.
(50) Fallah, K.; Norouzian Alam, S.; Ghaffary, B.; Yekekar, F.; Taghiyan, S.; Taravati, S. Enhancement of the Environmental Stability of Perovskite Thin Films via AZ5214-Photoresist and PMMA Coatings. *Opt Mater. Express* **2024**, *14* (8), 2083.
(51) Mallem, K.; Prodanov, M. F.; Dezhang, C.; Marus, M.; Kang, C.; Shivarudraiah, S. B.; Vashchenko, V. V.; Halpert, J. E.; Srivastava, A. K. Solution-Processed Red, Green, and Blue Quantum Rod Light-Emitting Diodes. *ACS Appl. Mater. Interfaces* **2022**, *14* (16), 18723−18735.
(52) Yuan, B.; Li, C.; Yi, W.; Juan, F.; Yu, H.; Xu, F.; Li, C.; Cao, B. PMMA Passivated CsPbI2Br Perovskite Film for Highly Efficient and Stable Solar Cells. *J. Phys. Chem. Solids* **2021**, *153*, No. 110000.
(53) Wang, Z.; He, H.; Liu, S.; Wang, H.; Zeng, Q.; Liu, Z.; Xiong, Q.; Fan, H. J. Air Stable Organic−Inorganic Perovskite Nanocrystals@Polymer Nanofibers and Waveguide Lasing. *Small* **2020**, *16* (43), No. 2004409.
(54) Kao, T. S.; Hong, K.-B.; Chou, Y.-H.; Huang, J.-F.; Chen, F.-C.; Lu, T.-C. Localized Surface Plasmon for Enhanced Lasing Performance in Solution-Processed Perovskites. *Opt Express* **2016**, *24* (18), 20696.
(55) Andalibi, M. R.; Wokaun, A.; Bowen, P.; Testino, A. Kinetics and Mechanism of Metal Nanoparticle Growth via Optical Extinction Spectroscopy and Computational Modeling: The Curious Case of Colloidal Gold. *ACS Nano* **2019**, *13* (10), 11510−11521.
(56) Yakubovsky, D. I.; Arsenin, A. V.; Stebunov, Y. V.; Fedyanin, D. Yu.; Volkov, V. S. Optical Constants and Structural Properties of Thin Gold Films. *Opt Express* **2017**, *25* (21), 25574.
(57) Haiss, W.; Thanh, N. T. K.; Aveyard, J.; Fernig, D. G. Determination of Size and Concentration of Gold Nanoparticles from UV−Vis Spectra. *Anal. Chem.* **2007**, *79* (11), 4215−4221.
(58) Hu, Y.-H.; Chen, C.-Y. The Effect of End Groups on the Thermal Degradation of Poly(Methyl Methacrylate). *Polym. Degrad. Stab.* **2003**, *82* (1), 81−88.
(59) Wang, S.; Ding, T. Plasmon-Assisted Nanojet Lithography. *Nanoscale* **2019**, *11* (19), 9593−9597.
(60) Wang, S.; Ding, T. Optical-Force-Directed Single-Particle-Based Track Etching in Polystyrene Films. *Nanotechnology* **2019**, *30* (30), No. 305304.
(61) Ding, T. Controllable Tuning of Fabry−Perot Cavities *via* Laser Printing. *J. Mater. Chem. C Mater.* **2020**, *8* (31), 10825−10830.
(62) Chegel, V.; Rachkov, O.; Lopatynskyi, A.; Ishihara, S.; Yanchuk, I.; Nemoto, Y.; Hill, J. P.; Ariga, K. Gold Nanoparticles Aggregation: Drastic Effect of Cooperative Functionalities in a Single Molecular Conjugate. *J. Phys. Chem. C* **2012**, *116* (4), 2683−2690.

https://doi.org/10.1021/acsanm.5c00832
ACS Appl. Nano Mater. 2025, 8, 8294−8306

(63) Zhang, L.; Salmain, M.; Liedberg, B.; Boujday, S. Naked Eye Immunosensing of Food Biotoxins Using Gold Nanoparticle-Antibody Bioconjugates. *ACS Appl. Nano Mater.* **2019**, *2* (7), 4150−4158.
(64) Khodaveisi, J.; Shabani, A. M. H.; Dadfarnia, S.; Saberi, D. A Novel Sensor for Determination of Naproxen Based on Change in Localized Surface Plasmon Peak of Functionalized Gold Nanoparticles. *Spectrochim Acta A Mol. Biomol Spectrosc* **2017**, *179*, 11−16.
(65) Wochnowski, C.; Shams Eldin, M. A.; Metev, S. UV-Laser-Assisted Degradation of Poly(Methyl Methacrylate). *Polym. Degrad. Stab.* **2005**, *89* (2), 252−264.
(66) Neumann, C.; Kaiser, D.; Mohn, M. J.; Füser, M.; Weber, N.-E.; Reimer, O.; Gölzhäuser, A.; Weimann, T.; Terfort, A.; Kaiser, U.; Turchanin, A. Bottom-Up Synthesis of Graphene Monolayers with Tunable Crystallinity and Porosity. *ACS Nano* **2019**, *13* (6), 7310−7322.
(67) Yao, J.; Li, Y.; Wang, S.; Ding, T. Thin-Film-Assisted Photothermal Deformation of Gold Nanoparticles: A Facile and In-Situ Strategy for Single-Plate-Based Devices. *ACS Nano* **2024**, *18* (15), 10618−10624.
(68) González-Rubio, G.; Guerrero-Martínez, A.; Liz-Marzán, L. M. Reshaping, Fragmentation, and Assembly of Gold Nanoparticles Assisted by Pulse Lasers. *Acc. Chem. Res.* **2016**, *49* (4), 678−686.
(69) Baffou, G.; Quidant, R. Thermo-plasmonics: Using Metallic Nanostructures as Nano-sources of Heat. *Laser Photon Rev.* **2013**, *7* (2), 171−187.
(70) Watzky, M. A.; Finke, R. G. Transition Metal Nanocluster Formation Kinetic and Mechanistic Studies. A New Mechanism When Hydrogen Is the Reductant: Slow, Continuous Nucleation and Fast Autocatalytic Surface Growth. *J. Am. Chem. Soc.* **1997**, *119* (43), 10382−10400.

https://doi.org/10.1021/acsanm.5c00832
ACS Appl. Nano Mater. 2025, 8, 8294−8306